Article

Enhanced Electrical Performance of Monolayer MoS$_2$ with Rare Earth Element Sm Doping

Shijie Li [1,2,†], Shidai Tian [1,2,†], Yuan Yao [1,2], Meng He [1,2], Li Chen [1,*], Yan Zhang [1,2,3,*] and Junyi Zhai [1,2,4,*]

1   Center on Nanoenergy Research, School of Physical Science and Technology, Guangxi University, Nanning 530004, China; lishijie@binn.cas.cn (S.L.); tianshidai@binn.cas.cn (S.T.); yaoyuan@binn.cas.cn (Y.Y.); hemeng@binn.cas.cn (M.H.)
2   CAS Center for Excellence in Nanoscience, Beijing Key Laboratory of Micro-Nano Energy and Sensor, Beijing Institute of Nanoenergy and Nanosystems, Chinese Academy of Sciences, Beijing 100083, China
3   School of Physics, University of Electronic Science and Technology of China, Chengdu 610054, China
4   College of Nanoscience and Technology, University of Chinese Academy of Science, Beijing 100049, China
*   Correspondence: chenli@gxu.edu.cn (L.C.); zhangyan@uestc.edu.cn (Y.Z.); jyzhai@binn.cas.cn (J.Z.)
†   These authors contributed equally to this work.

Abstract: Rare earth (RE) element-doped two-dimensional (2D) transition metal dichalcogenides (TMDCs) with applications in luminescence and magnetics have received considerable attention in recent years. To date, the effect of RE element doping on the electronic properties of monolayer 2D-TMDCs remains unanswered due to challenges including the difficulty of achieving valid monolayer doping and introducing RE elements with distinct valence and atomic configurations. Herein, we report a unique strategy to grow the Sm-doped monolayer MoS$_2$ film by using an atmospheric pressure chemical vapor deposition method with the substrate face down on top of the growth source. A stable monolayer triangular Sm-doped MoS$_2$ was achieved. The threshold voltage of an Sm-doped MoS$_2$-based field effect transistor (FET) moved from -12 to 0 V due to the p-type character impurity state introduced by Sm ions in monolayer MoS$_2$. Additionally, the electrical performance of the monolayer MoS$_2$-based FET was improved by RE element Sm doping, including a 500% increase of the on/off current ratio and a 40% increase of the FET's mobility. The electronic property enhancement resulted from Sm doping MoS$_2$, which led internal lattice strain and changes in Fermi energy levels. These findings provide a general approach to synthesize RE element-doped monolayer 2D-TMDCs and to enrich their applications in electrical devices.

Keywords: monolayer MoS$_2$; CVD growth; Sm doping; electrical performance; FET

1. Introduction

In recent years, there has been an increasing interest in two-dimensional (2D) transition metal dichalcogenides (TMDCs) due to their unique properties and great potential for electronic and optoelectronic applications [1,2]. 2D-TMDCs are a kind of low-dimensional materials that have the formula of MX$_2$, where M stands for the transition-metals like Mo, W, and Ti, and X represents S, Se, and Te [3]. Nevertheless, the characteristics presented by 2D-TMDCs are extremely monotonous and limited [4]. Realizing the full potential of 2D-TMDCs in high-performance thin film transistors and to endow some new distinguishing features requires some doping strategies to effectively control their carrier type and to modulate the band gap [5]. Common doping strategies for 2D-TMDCs include substitution doping during growth, ion implantation, and surface charge transfer [6]. However, in these previous doping schemes, ion injection and surface charge transfer in monolayer 2D-TMDC doping were often not stable enough, thus limiting their application [6,7]. Substitution the doping of 2D-TMDCs has been widely explored for materials applications in electronic and optoelectronic [7], as well as room-temperature ferromagnetism, applications [8–10]. Transition elements have been used as cationic substitutes for doped 2D-TMDCs, e.g.,

the Nb ion-doped 2D-TMDCs achieving p-type [7] transport characteristics and the Re ion-doped 2D-TMDCs achieving nearly degenerate n-type doping [11]. Moreover, in recent studies, Fu's group confirmed ferromagnetism in monolayer MoS_2 via in situ Fe-doping at room temperature [10] and Pham's group enhanced tunable ferromagnetism in V-doped WSe_2 monolayers at 0.5–5 at% V concentrations [9]. Additionally, other transition metal elements in the in situ substitution of MoS_2-doped for electronic application studies have been demonstrated, such as for Mn [12]. The above research had demonstrated that the doping of transition metal elements is able to tune the electrical, optical, and magnetic properties of 2D-TMDCs [13]. Thus far, transition metal elements have been widely demonstrated in in situ substitution-doped monolayer 2D-TMDCs. However, the doping engineering of atomically thin TMDCs by introducing elements with different atomic valences and atomic configurations, such as RE elements, is still challenging. Currently, a range of difficult issues still exists for in situ RE element substitution-doped large monolayer 2D-TMDCs.

RE elements, which usually exist as trivalent cations, are composed of 15 lanthanides (from lanthanum to lutetium), plus scandium and yttrium [14]. In previous studies, it could be noted that RE ions were commonly doped in traditional insulator or semiconductors [15]. RE elements can also be used as efficient dopants in TMDC materials. Lanthanide (Ln) ions have a rich f-orbit configuration that allows them to absorb and emit photons from the ultraviolet to infrared region via the $4f$-$4f$ or $4f$-$5d$ transition, making them candidates for extended 2D-TMDC semiconductor luminescence [15,16]. In addition, RE dopants with unfilled $4f$ energy states and charge-transfer state structures may provide strong spin-orbit coupling to tune the semiconductor properties of the 2D-TMDC's host material [17]. Furthermore, first principle calculations confirmed the possibility of doping 2D-TMDCs with rare earth elements [18,19]. Currently, progress is being made in the study of RE element-doped 2D-TMDCs films for optical, electronic, and magnetic applications [20]. For example, Qi Zhao et al. made a breakthrough to synthesize MoS_2:Dy sheets with robust and adjustable ferromagnetic properties at room temperature by a gas–liquid chemical deposition method [17]. Gongxun Bai et al. synthesized a novel 2D system of an Er-doped multilayer MoS_2 to study NIR-to-NIR down-and up-conversion photoluminescence [16]. However, these studies were based on some thicker-layer 2D-TMDC materials. Later on, Yongxin Lyu et al. fabricated Er-embedded MoS_2 triangle islands along the in-plane size of up to around 10 μm, which apparently formed single crystals [21]. Additionally, Fu et al. used a salt-assisted sustained-release chemical vapor deposition (CVD) method to grow Eu ion-doped MoS_2 [22]. Their methods yielded smaller sized samples and tended to introduce new dopant impurities. In addition, Eu and Er element-doped 2D-TMDC research has focused on photoluminescence and ferromagnetic properties, with little reported on the electrical properties of other rare earth element-doped monolayer 2D-TMDCs. Therefore, it is unclear whether the introduction of rare earth elements into monolayer 2D-TMDCs can effectively control their carrier type and regulate carrier concentration.In this work, we demonstrate a large-sized MoS_2 film doped with the RE element Sm by an atmospheric pressure, three-zone CVD method. In addition, stable monolayer triangular Sm-doped MoS_2 films were obtained at the edge positions of the large size films.

MoS_2 was chosen as the doping host material because it is a typical example from the layered 2D-TMDC family of materials [23]. Additionally, Sm is more economic compared to Er and Eu elements when investing in the optimization conditions for rare earth element-doped monolayer 2D materials by CVD. The monolayer MoS_2 was used as a matrix material to embed Sm, as confirmed by characterization methods such as Raman, photoluminescence (PL), X-ray photoelectron spectroscopy (XPS), atomic force microscope (AFM), and energy dispersive X-ray spectroscopy (EDS) elemental mapping. As the monolayer triangle MoS_2 was found to be the most energetically stable existent morphology, we characterized the electrical properties of stable triangular MoS_2 field effect transistor (FET) before and after its doping. Electrical measurements showed that Sm element doping led to considerable changes in the electronic band structure of the host MoS_2.The doping of

Sm may lead to a non-uniform charge distribution, suppress the n-type characteristic, and change the energy band structure of MoS_2.

2. Materials and Methods

2.1. Synthesis of the Sm-Doped MoS$_2$ Film on a SiO$_2$/Si Substrate by the CVD System

The three-zone CVD system is composed of two parts—an external temperature zone heated by a heating belt and the two temperature zones of a furnace. Alcohol/isopropanol/ deionized water and a 3:1 mix solution of concentrated H_2SO_4 and H_2O_2 were used in this study for the pretreatment of the 270 nm-thick, SiO_2-capped Si substrate before Sm-doped MoS_2 growth by CVD [24]. Sublimed sulfur powder (Aladdin, Shanghai, China, 99.5%; 900 mg), MoO_3(VI) powder (Alfa, Louis, MO, USA, 99.5%; 10 mg), and $SmCl_3 \cdot 6H_2O$ particles (Macklin, Shanghai, China, 99%; 5 mg) were loaded in three customized crucible lids before growth and placed in the quartz tube of the furnace, as shown in the Supplementary Materials (Figure S1).

Then, the different samples in the three-crucible lid were fed by a tool into the corresponding positions of the quartz tube. First, the SiO_2/Si (1 cm × 2 cm) substrate that was placed upside down on top of the MoO_3 powder crucible lid was placed in the second zone of the furnace. Second, the $SmCl_3 \cdot 6H_2O$ particle was put in the first zone of the furnace. Third, sulfur powder was located at the external temperature zone. The temperature and Ar gas flow control procedure for CVD-doped growth is as follows. After purging the furnace with Ar for 20 min [25], the temperature of the two temperature zones of the tube furnace itself was ramped to 100 °C in 20 min and maintained for 30 min, while the carrier gas flow rate in this process was 200 sccm. The subsequent steps in the temperature and Ar gas flow control procedure were that the first and second temperature zones of the furnace were increased from 100 to 800 and 750 °C, respectively, within 53 min and then maintained for 30 min. The Ar gas flow rate changed from 200 to 100 sccm when heating up from 100 °C. Additionally, the S powder was heated by a heating belt when the first zone of the furnace was heated to 650 °C. After the thermal growth process ended, the furnace and heating belt were allowed to naturally cool down to room temperature [26].

2.2. FET Device Fabrication

The FET device preparation is divided into two main parts: sample transfer and source and drain electrode preparation [27,28]. During the transfer process, a thin layer of poly methyl methacrylate (PMMA) was spun-coated on the CVD-grown, Sm-doped MoS_2 and then baked for 3 min at 150 °C. Next, the excess non-sample area was removed, and the remaining sample coated by the PMMA was immersed in 20% Hydrofluoric acid solution to etch SiO_2. At the end, the detached film was cleaned in deionized water several times and transferred to the heavily doped SiO_2/Si substrate. Next was the process of preparing the electrodes for the FET device. First, the residual PMMA covering the transfer sample on the target substrate was removed with an acetone solution. Second, a new thin layer of PMMA was spun-coated on the CVD-grown, Sm-doped MoS_2, and then the electrodes were exposed in the appropriate positions via electron beam lithography (EBL) according to the designed electrode pattern. Third, Cr/Au (10 nm/50 nm) of the source and drain electrodes was deposited in the corresponding position by electron beam eVaporation deposition. In SiO_2/Si substrates, Cr/Au (10 nm/50 nm) electrode plating was also required for Si as a gate voltage. Finally, the acetone solution removed the PMMA, and the corresponding device was obtained on the substrate.

2.3. Characterization

Raman and PL spectra were taken by a LabRAM HR eVolution system (HORIBA Co. Ltd., Paris, France) with a 532 nm laser. The Raman spectroscopy parameters were a diffraction grating of 1800 gr/mm, a focal length of 800 mm, a Raman frequency shift range of 50–8000 cm^{-1}, and a spectral resolution of ≤ 0.65 cm^{-1}. The morphology of fabricated devices and the morphology of as-grown Sm-doped MoS_2 were observed by

a fluorescent inverted microscope (LeicaDMI6000B, Leica, Hesse-Darmstadt, Germany), and the thickness of few-layer flakes was characterized by AFM (MFP-3D-SA, Asylum Research, Santa Barbara, CA, USA) and Raman spectroscopy. The electrical properties of all the FET devices were measured using a Keithley 4200 (Tektronix, Beaverton, OR, USA) semiconductor parameter analyzer at room temperature (under dark conditions). XPS was conducted on a Thermo Scientific^{TM} K-Alpha^{TM+}(Thermo Scientific, Waltham, MA, USA) spectrometer equipped with a monochromatic Al Kα X-ray source (1486.6 eV) operating at 100 W. Samples were analyzed under vacuum ($p < 10^{-8}$ mbar) with a pass energy of 150 eV (survey scans) or 25 eV (high-resolution scans). All peaks would be calibrated with C1s peak binding energy at 284.8 eV for adventitious carbon. The experimental peaks were fitted with the Avantage software. TEM images were obtained with an FEI Talos F200X (Thermo Scientific, Waltham, MA, USA)

3. Results and Discussion

3.1. Fabrication of Monolayer Sm-Doped MoS$_2$

The monolayer Sm-doped MoS$_2$ film was directly synthesized by the three-zone CVD system of atmospheric pressure method on the SiO$_2$/Si substrate that was placed face down [29] on the crucible lid in a quartz tube, and the overall process of the growth system is illustrated in Figure 1a. As Figure 1a shows, sulfur powder was placed upstream, and the SmCl$_3$·6H$_2$O particle was placed in the middle of the S and MoO$_3$ powder. In the synthetic process, SmCl$_3$ has two effects: one is as a dopant, and the other is as an assistant agent for the long-distance transmission of MoO$_{3-x}$ [24]. Additionally, the SiO$_2$/Si (1 × 2 cm) substrate that was placed upside down on top of the MoO$_3$ powder crucible lid was downstream of the furnace. Figure 1b shows an enlarged growth model processes for the synthesis of monolayer Sm-doped MoS$_2$ on the SiO$_2$/Si substrate facing down on the MoO$_3$ powder. Figure 1c,d exhibits the optical images of the monolayer triangular MoS$_2$ and Sm-doped MoS$_2$, respectively. The size of CVD-grown, Sm-doped MoS$_2$ triangle islands along the in-plane was up to around 50 µm. More optical images can be seen in Figure S2. The triangle MoS$_2$ was the most energetically stable existent morphology, and the uniformity of the obtained large-size films was not as good as that of the triangle MoS$_2$. The specific analysis can be seen in the Supplementary Materials (Figure S3).
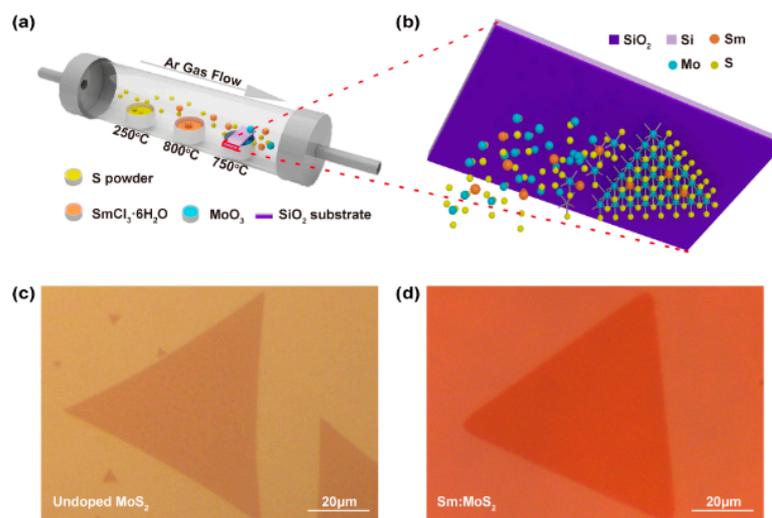
Figure 1. The growth of monolayer triangular Sm-doped MoS$_2$ film. (**a**) Schematic of the three-temperature zone chemical vapor deposition (CVD) system for the growth of the monolayer Sm-doped MoS$_2$ film on the SiO$_2$/Si substrate. (**b**) The simple growth model processes for the synthesis of monolayer triangular Sm-doped MoS$_2$ on SiO$_2$/Si substrate. Optical microscopy images of (**c**) undoped and (**d**) Sm-doped monolayer triangular MoS$_2$. Scale bar = 20 µm.

3.2. Characterizations and Analysis of Monolayer Sm-Doped MoS$_2$

3.2.1. Raman and Photoluminescence Analysis of Monolayer Sm-Doped MoS$_2$

Raman spectroscopy was performed to investigate the layers of the MoS$_2$ and Sm-doped MoS$_2$, and PL spectroscopy was employed to demonstrate the doping effect. Figure 2a shows the Raman spectra of MoS$_2$ and Sm-doped MoS$_2$, where the Raman spectrum of Sm-doped MoS$_2$ can be seen to have exhibited two typical characteristic vibration modes of layered MoS$_2$ at E_{2g}^1 = 384.6 cm^{-1} (in-plane vibration of Mo and S atoms) and A$_{1g}$ = 404.5 cm^{-1} (out-of-plane vibration of S atoms). The peak spacing between the E_{2g}^1 and A$_{1g}$ was 19.9 cm^{-1}, suggesting the MoS$_2$ and Sm-doped MoS$_2$ were monolayers [30]. Figure S4b,d shows an AFM image of the Sm-doped MoS$_2$ and undoped MoS$_2$ samples, respectively. The height profiles indicate that the thickness of a typical flake was approximately 0.83 nm, which was almost comparable to that of the single layer MoS$_2$ crystal. Additionally, both vibrational modes of Sm-doped MoS$_2$ are displayed in a small blue shift compared with the monolayer MoS$_2$, implying the possible effects of the Sm doping and/or the presence of defects on MoS$_2$ [16]. Due to the competing effects of lattice strain and Sm^{3+} charge doping on the Raman shift, the overall blue shift of the A$_{1g}$ and E_{2g}^1 peak was relatively small [31]. Furthermore, the distortion of the MoS$_2$ lattice could give rise to the optical quenching of the PL intensities [10]. It can be seen from Figure 2b that undoped MoS$_2$ had a strong PL peak at about 1.82 eV, implying the MoS$_2$ is a direct band gap semiconductor. However, the PL intensities of Sm-doped MoS$_2$ were observed to be much lower with a 30 meV blue shift than that of undoped MoS$_2$, which was consistent with previous predictions of the optical quenching of the PL intensities due to distortion of the MoS$_2$ lattice [10]. This may be ascribed to the introduction of new defects due to lattice distortion by the doped Sm ions, as well as changes in band gap width. Using the equation $\delta\omega = 2\gamma\omega_0\varepsilon$ [32] and band gap deformation potential, it was found that the lattice strains arising from the Sm doping were about 0.076% and 0.1%, respectively. This was also confirmed in the previous studies of lanthanide Er-doped [16] MoS$_2$ and Eu-doped [22] MoS$_2$. Additionally, the Raman mapping corresponding to the E_{2g}^1 and A$_{1g}$ peaks was used to confirm the uniformity growth of the monolayer triangular samples with and without Sm doping, as shown in Figure 2d,e,g,h, respectively. It was observed that the Sm-doped monolayer MoS$_2$ showed a more regular triangular shape and a more uniform peak distribution than undoped MoS$_2$. Thus, Sm doping improved the homogeneity of the sample.

3.2.2. XPS Spectrum Analysis of Monolayer Sm-Doped MoS$_2$

XPS was performed to investigate the elements and valence state information of monolayer MoS$_2$ and Sm-doped MoS$_2$. Figure 3a–c displays the comparisons of XPS results from the undoped MoS$_2$ (in black) and Sm-doped MoS$_2$ (in red). In the full spectrum (Figure 3a), there are Si, O, and C core levels in addition to S and Mo core levels. The Si and O core levels in the samples may have come from the SiO$_2$/Si substrate, so the O peak intensity was much higher than that of C. The core level of Sm was only found in the Sm-doped MoS$_2$. Additionally, the spectral shape of the S and Mo core levels after Sm-doping was nearly identical to that of the undoped MoS$_2$, which indicated that Sm-doping did not significantly chemically alter the MoS$_2$ host [33]. However, compared to the undoped sample, it was obvious that the doped S 2p and Mo 3d core level peaks were both shifted by 0.18 eV towards the lower binding energies. The specific displacement changes of the binding energy were as follows: Mo 3d$_{3/2}$ shifted from 232.64 to 232.82 eV, Mo 3d$_{5/2}$ shifted from 229.7 to 229.52 eV, S 2p$_{1/2}$ shifted from 163.74 to 163.56 eV, and S 2p$_{3/2}$ shifted from 162.54 to 162.36 eV [34]. The slight shift indicated the change of chemical microenvironment around these atoms for Sm-doped MoS$_2$ materials [22]. It can be inferred that the binding energy shifts were associated with Fermi level shifts and originated from the incorporation of Sm into MoS$_2$ single crystals [16,22]. The binding energy shift direction and magnitude of Sm-doped MoS$_2$ were also found to be consistent with the variation of p-type-doped MoS$_2$ [16]. As seen in Figure 3d, the obvious binding energy peaks related to the Sm 3d$_{5/2}$

at 1083.58 eV [35] indicated that the Sm ions were trivalent [36], but the Sm $3d_{3/2}$ did not have a significant peak. That may be attributed to the low concentration of Sm, with XPS estimating a doping concentration of about 1.1at%.

3.2.3. TEM Analysis of Monolayer Sm-Doped MoS$_2$

TEM was carried out to further investigate the microstructure and elemental composition of the monolayer Sm-doped MoS$_2$. The EDS elemental mapping images of S, Mo, and Sm in Sm-doped monolayer MoS$_2$, which were taken from the area shown in Figure 4a, are shown in Figure 4b–d. Though the S, Mo, and Sm elemental mapping image scans were complete, the amount of detected Sm element was small. This indicated the existence of a low doping concentration of Sm in the monolayer MoS$_2$. The elemental Sm doping concentration of the selected area detected by EDS (Figure S5) was about 1.42at%. In Figure S5, selected area electron diffraction (SAED) patterns indicate that Sm doping did not change the original crystal structure.
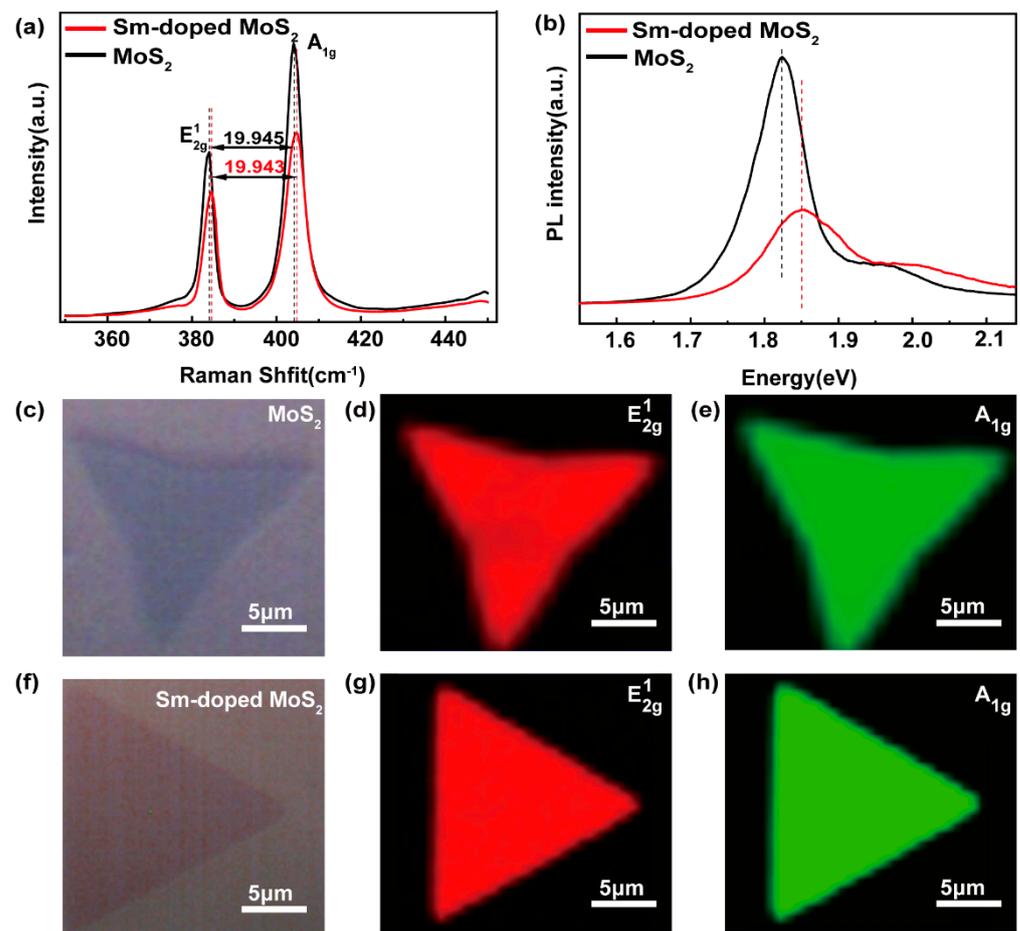
Figure 2. (**a**) Raman spectra and (**b**) photoluminescence (PL) spectra of monolayer triangular MoS$_2$ and Sm-doped triangular MoS$_2$ under 532 nm laser excitation. The (**c**) and (**f**) plots show the MoS$_2$ and Sm-doped MoS$_2$ optical microscopy images under Raman detection, respectively. (**d**,**e**,**g**,**h**) Raman mappings of the peak position corresponding to E$_{2g}^1$ and A$_{1g}$ of the MoS$_2$ and Sm-doped MoS$_2$, respectively. Raman and PL spectroscopy were conducted using a confocal Raman microscope with a 532 nm laser at room temperature.
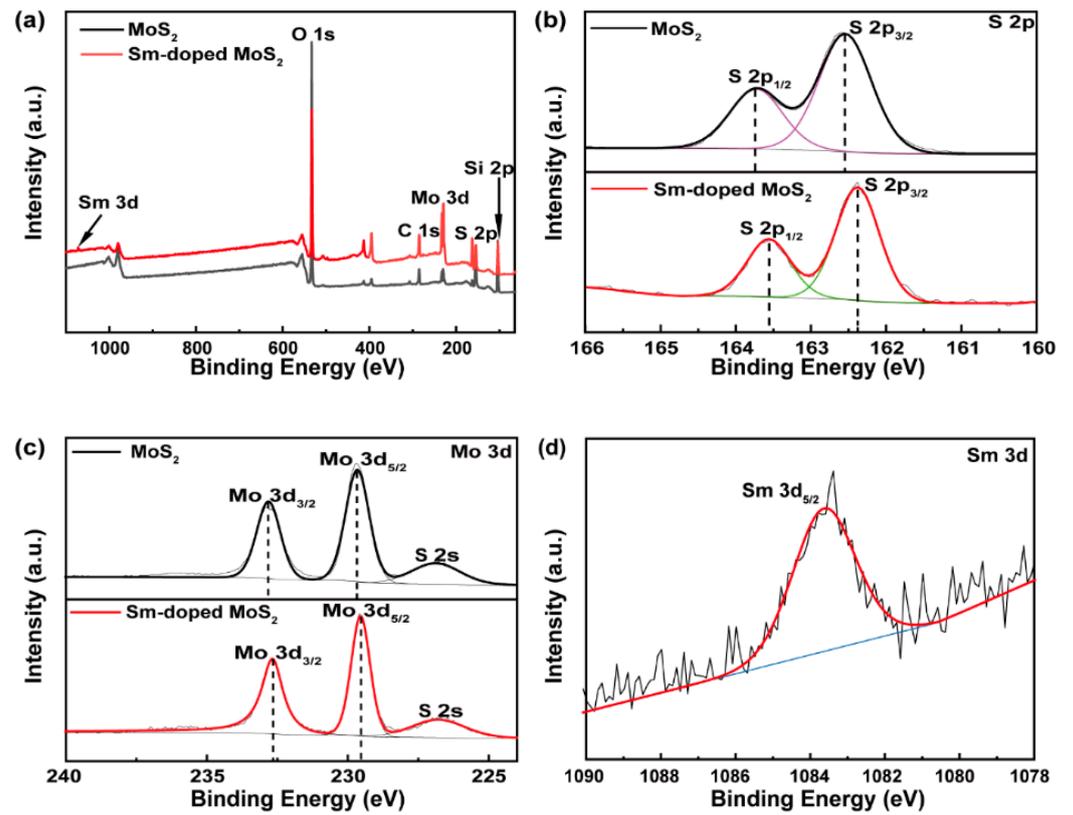
Figure 3. XPS spectrum (**a**) total scans, (**b**) S 2p, (**c**) Mo 3d, and (**d**) Sm 3d core levels.
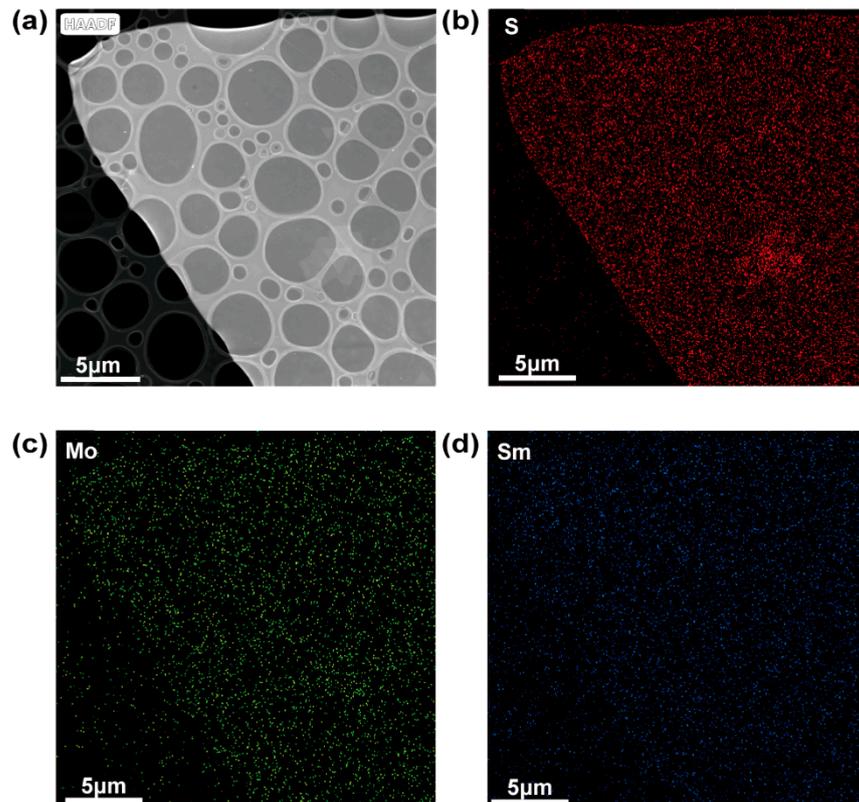
Figure 4. TEM characterizations of Sm-doped MoS_2. (**a**) Low resolution TEM area of EDS mapping. (**b**–**d**) EDS elemental mapping images of S, Mo, and Sm in Sm-doped MoS_2, respectively.

3.3. Electrical Properties Characterisation of Monolayer Sm-Doped MoS$_2$ FET

In order to investigate the electrical properties of the Sm-doped monolayer MoS$_2$, a bottom gate FET was fabricated on the SiO$_2$/Si substrate with Cr/Au (10/50 nm) as the source and drain electrodes as shown in Figure 5a. The SiO$_2$ layer thickness of the FET devices was 285 ± 20 nm. Specifically, the electrical performance of the FET devices was tested in the dark. Figure 5b shows the output curves of Sm-doped (red) and undoped (black) monolayer MoS$_2$ at a gate voltage of 10 V. The inset shows a microscopy image of the FET under the light microscope. It is clear that the output characteristics of monolayer MoS$_2$ were better than those of Sm doping under the same conditions, implying the restraint of electrical conductivity with Sm doping. This was due to the fact that the Sm element caused distortions in the lattice structure near the doping site, resulting in an inhomogeneous charge density distribution. Figure 5c,d shows the transfer curves of an MoS$_2$ FET with and without Sm doping. The undoped MoS$_2$ FET displayed typical n-type transport characteristics (black), as previously reported in the literature [23,37–39]. Compared to undoped MoS$_2$ (red), the threshold voltage (V_{th}) of Sm-doped MoS$_2$ moved from −12 to 0 V, as seen in Figure 5c. It can also be seen in Figure 5d that the inflection point of the transfer curve of the doped MoS$_2$ shifted to a more positive gate voltage with respect to the inflection point of the undoped MoS$_2$, implying a Fermi level closer to the valence band maximum (VBM) by Sm doping. More V_{ds} transfer characteristics of Sm-doped MoS$_2$ FET devices are shown in Figure S6 in the Supplementary Materials, where it can be seen that the V_{th} for doping all showed a tendency to shift towards a more positive gate voltage. The positive shift of the V_{th} was consistent with the p-type dopant behavior of in MoS$_2$ [40]. This was because during the Sm substitution doping process, the Sm 4*f* states contributed to the formation of a valence band and a hybridization of Sm 4*f* and Mo 4*d* on the edge of the valence band. This brought the Fermi energy level close to the valence band, leading to p-type doping. Furthermore, this was also coherent with the p-type doping conclusion obtained from the core energy level of XPS that shifted towards a lower binding energy. However, significant p-type (hole-transport) behavior of MoS$_2$ devices was not observed, presumably due to the Fermi-level pinning of the Cr/Au contact metal close to the conduction band of MoS$_2$ [33,41] or a smaller shift in the Fermi energy level caused by a smaller doping concentration. Figure 5e, f shows the band alignment diagrams and the formation of the Schottky barrier (SB) before and after doping. The figure shows the schematic of an energy diagram of a Cr/Au electrode and an MoS$_2$ monolayer where the work functions of Cr (Φ_{Cr}) and Au (Φ_{Au}) were 4.5 and 5.1 eV, respectively [38], and the electron affinity (χ) of MoS$_2$ was ~4.2 eV [42]. The energy band of the MoS$_2$ bended upon contact to form the SB (blue line). Sm doping in MoS$_2$ caused the Fermi energy to shift closer to the VBM and the impurity level to be close to the VBM. Additionally, an empty Sm 4*f* state was present at the bottom of the conduction band. All of this led to the Fermi energy level being closer to valence band and an increase the height of the SB$_{Sm}$, as well as a decrease in device current. Moreover, this corresponded to the actual measured electrical properties. The field-effect mobility (μ_{FE}) could be calculated from transfer curve (Figure 5d) according to the following equation [39]:

$$\mu_{FE} = \frac{dI_{ds}}{dV_g} \cdot \frac{L}{W} \cdot \frac{1}{C_g \cdot V_d} \tag{1}$$

$$C_g = \frac{\varepsilon_0 \varepsilon_r}{d} \tag{2}$$

where dI_{ds}/dV_g is the slope of the transfer curve; L and W are the length and width of the channel, respectively; V_d is the drain voltage; C_g is area-normalized capacitance of 280 nm-thick SiO$_2$; ε_0 is vacuum dielectric constant; ε_r is relative dielectric constant; and d is the SiO$_2$ thickness. The calculation gave mobility values of 4.35 and 3.08 cm^2/Vs for Sm-doped and undoped uncased monolayer FETs, respectively. Furthermore, the on/off current ratio for V_g ranged from −30 to +30 V, with a source-drain bias of 0.5 V for the Sm-doped monolayer MoS$_2$ FET of about 3×10^4, which was higher than that of the

undoped monolayer MoS_2—5×10^3. This represented a 500% improvement in the on/off performance of the doped device, but the change in migration rate was not very significant. The I_{ds}–V_g curve in Figure 5c indicates that the FET made of Sm-doped MoS_2 showed a current density close to the MoS_2 FET at the "on" state but a much lower current density (1000 times lower) at the "off" state. These results suggested that Sm doping reduced the electron density in MoS_2 and led to a small I_{off}. As a result, both the radius difference and concentration of impurities can affect the electrical properties of monolayer MoS2. This is because the lattice distortion caused by the doped atoms can change the energy band structure of monolayer MoS_2 and affect the charge distribution, and the doping concentration determines the variation in band gap width and Femi energy level.
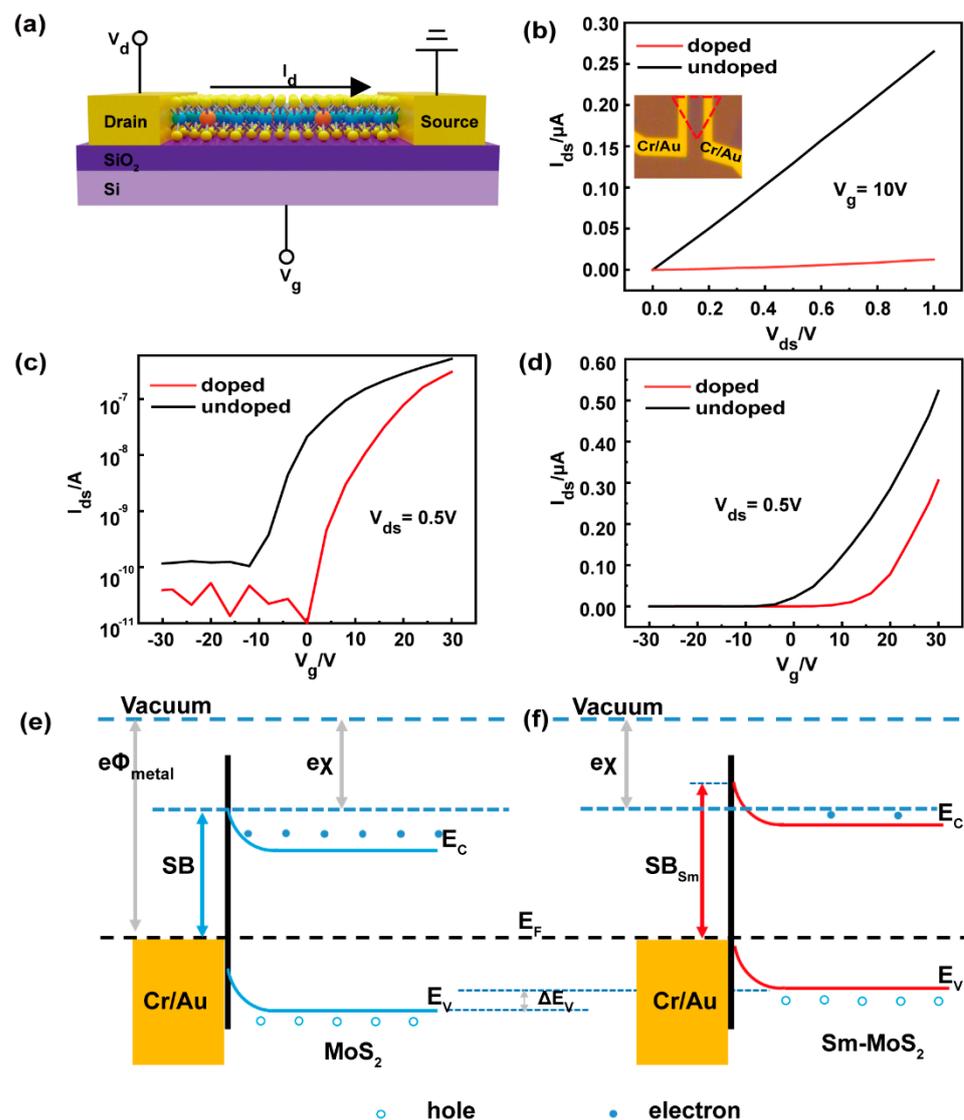
Figure 5. Electrical properties of monolayer MoS_2 and Sm-doped MoS_2. (**a**) The schematic drawing of a Sm-doped monolayer MoS_2 FET. (**b**) Output curves (I_{ds}–V_{ds}) of MoS_2 and Sm-doped MoS_2 devices at a gate bias of 10 V. The inset is the topography of the device. (**c**) Source-drain current (I_{ds}) vs gate voltage (V_g) characteristics of monolayer MoS_2 and the Sm-doped MoS_2 FET device at a drain voltage (V_{ds}) of 0.5 V on a log scale. (**d**) Transfer curves (I_{ds}–V_g) of monolayer MoS_2 and the Sm-doped MoS_2 FET device with a V_g from −30 to 30 V. Band alignment diagrams and the formation of the Schottky barrier after contact between the Cr/Au electrode and (**e**) pristine MoS_2 (blue line) and (**f**) Sm-doped MoS_2 (red line).

4. Conclusions

In conclusion, Sm-doped monolayer triangular MoS_2 was successfully grown by CVD, which was confirmed to be monolayer by Raman and AFM measurements. FET devices were fabricated with the Sm-doped monolayer triangular MoS_2, and its V_{th} was shifted from -12 to 0 V compared to be undoped, MoS_2-based FETs. The positive shift change in V_{th} was attributed to the fact that Sm acted as substitutional p-type dopant in MoS_2, consistent with theoretical predictions and XPS analysis. The 500% increase in the on/off current ratio of Sm-doped devices was due to the reduction of the electron density in MoS_2 after Sm ion doping, which also led to a small I_{off}. This was due to the lattice strain caused by Sm doping. The above results show that RE element Sm substitutional doping can tune and enhance the electrical properties of monolayer MoS_2. This study opens up a wide range of applications for tuning the electrical properties of monolayer 2D-TMDCs by doping with RE elements.

Supplementary Materials: The following are available online at https://www.mdpi.com/2079-4991/11/3/769/s1. Figure S1: Schematic of the CVD system for growth of monolayer Sm-doped MoS_2 film on SiO_2/Si substrate. Figure S2: Optical image of triangular monolayer Sm-doped MoS_2. Figure S3: Disordered and irregular films during CVD doping growth and the respective corresponding Raman spectra. Figure S4: Optical microscopy images of (a) Sm-doped and (c) undoped MoS_2 triangles. AFM images and the height of (b) Sm-doped and (d) undoped MoS_2. Figure S5. (a) Low-magnification TEM image of Sm-doped MoS_2 single crystal on a Cu grid. SAED patterns (b,c) collected from different sites on the monolayer triangle Sm-doped MoS_2. (d) Low-magnification TEM image of Sm-doped MoS_2; the red box shows the measured area of figure (e). EDS spectrum (e) of Sm-doped MoS_2 with Mo, Sm, and S labels and inset showing the atomic percent of labeled elements. Inset: partial enlargement. Figure S6: (a) Photomicrograph of the FET device. (b) Transfer curves (I_{ds}–V_g) of monolayer MoS_2 FET device at drain voltages (V_{ds}) of 0.1, 1, and 2 V with V_g varying from -30 to 30 V. (c) Transfer curves (I_{ds}–V_g) of monolayer Sm-doped MoS_2 FET device at drain voltages (V_{ds}) of 0. 1, 1, and 2 V with V_g varying from -30 to 30 V. Transfer curves (I_{ds}–V_g) comparing of monolayer MoS_2 and Sm-doped MoS_2 at drain voltages (V_{ds}) 2 V (d), 1 V (e), and 0. 1 V (f) with V_g varying from -30 to 30 V.

Author Contributions: Conceptualization, S.L., L.C., and J.Z.; methodology, S.L. and Y.Y.; validation, S.L., S.T., and M.H.; formal analysis, S.L. and S.T.; investigation, S.L. and S.T.; writing—original draft preparation, S.L.; writing—review and editing, S.L., L.C., Y.Z., and J.Z.; supervision, L.C., Y.Z., and J.Z.; project administration, L.C., Y.Z., and J.Z.; funding acquisition, L.C., Y.Z., and J.Z. All authors have read and agreed to the published version of the manuscript.

Conflicts of Interest: The authors declare no conflict of interest.

References

1. Wang, Q.H.; Kalantar-Zadeh, K.; Kis, A.; Coleman, J.N.; Strano, M.S. Electronics and optoelectronics of two-dimensional transition metal dichalcogenides. *Nat. Nanotechnol.* **2012**, *7*, 699–712. [CrossRef] [PubMed]
2. Zhang, K.; Feng, S.; Wang, J.; Azcatl, A.; Lu, N.; Addou, R.; Wang, N.; Zhou, C.; Lerach, J.; Bojan, V.; et al. Manganese Doping of Monolayer MoS_2: The Substrate Is Critical. *Nano Lett.* **2015**, *15*, 6586–6591. [CrossRef]
3. Wang, Y.; Tseng, L.-T.; Murmu, P.P.; Bao, N.; Kennedy, J.; Ionesc, M.; Ding, J.; Suzuki, K.; Li, S.; Yi, J. Defects engineering induced room temperature ferromagnetism in transition metal doped MoS_2. *Mater. Des.* **2017**, *121*, 77–84. [CrossRef]
4. Li, W.; Huang, J.; Han, B.; Xie, C.; Huang, X.; Tian, K.; Zeng, Y.; Zhao, Z.; Gao, P.; Zhang, Y.; et al. Molten-Salt-Assisted Chemical Vapor Deposition Process for Substitutional Doping of Monolayer MoS_2 and Effectively Altering the Electronic Structure and Phononic Properties. *Adv. Sci.* **2020**, *7*, 2001080. [CrossRef] [PubMed]
5. Tang, J.; Wei, Z.; Wang, Q.; Wang, Y.; Han, B.; Li, X.; Huang, B.; Liao, M.; Liu, J.; Li, N.; et al. In Situ Oxygen Doping of Monolayer MoS_2 for Novel Electronics. *Small* **2020**, *16*, 2004276. [CrossRef]

6. Zhao, Y.; Xu, K.; Pan, F.; Zhou, C.; Zhou, F.; Chai, Y. Doping, Contact and Interface Engineering of Two-Dimensional Layered Transition Metal Dichalcogenides Transistors. *Adv. Funct. Mater.* **2017**, *27*, 1603484. [CrossRef]

7. Qin, Z.; Loh, L.; Wang, J.; Xu, X.; Zhang, Q.; Haas, B.; Alvarez, C.; Okuno, H.; Yong, J.Z.; Schultz, T.; et al. Growth of Nb-Doped Monolayer WS2 by Liquid-Phase Precursor Mixing. *ACS Nano* **2019**, *13*, 10768–10775. [CrossRef] [PubMed]

8. Zhang, F.; Zheng, B.; Sebastian, A.; Olson, D.H.; Liu, M.; Fujisawa, K.; Pham, Y.T.H.; Jimenez, V.O.; Kalappattil, V.; Miao, L.; et al. Monolayer Vanadium-Doped Tungsten Disulfide: A Room-Temperature Dilute Magnetic Semiconductor. *Adv. Sci.* **2020**, *7*, 2001174. [CrossRef] [PubMed]

9. Pham, Y.T.H.; Liu, M.; Jimenez, V.O.; Yu, Z.; Kalappattil, V.; Zhang, F.; Wang, K.; Williams, T.; Terrones, M.; Phan, M.H. Tunable Ferromagnetism and Thermally Induced Spin Flip in Vanadium-Doped Tungsten Diselenide Monolayers at Room Temperature. *Adv. Mater.* **2020**, *32*, 2003607. [CrossRef] [PubMed]

10. Fu, S.; Kang, K.; Shayan, K.; Yoshimura, A.; Dadras, S.; Wang, X.; Zhang, L.; Chen, S.; Liu, N.; Jindal, A.; et al. Enabling room temperature ferromagnetism in monolayer MoS2 via in situ iron-doping. *Nat. Commun.* **2020**, *11*, 2034. [CrossRef] [PubMed]

11. Zhang, K.; Bersch, B.M.; Joshi, J.; Addou, R.; Cormier, C.R.; Zhang, C.; Xu, K.; Briggs, N.C.; Wang, K.; Subramanian, S.; et al. Tuning the Electronic and Photonic Properties of Monolayer MoS2 via In Situ Rhenium Substitutional Doping. *Adv. Funct. Mater.* **2018**, *28*, 1706950. [CrossRef]

12. Cai, Z.; Shen, T.; Zhu, Q.; Feng, S.; Yu, Q.; Liu, J.; Tang, L.; Zhao, Y.; Wang, J.; Liu, B.; et al. Dual-Additive Assisted Chemical Vapor Deposition for the Growth of Mn-Doped 2D MoS2 with Tunable Electronic Properties. *Small* **2020**, *16*, 1903181. [CrossRef]

13. Feng, S.; Lin, Z.; Gan, X.; Lv, R.; Terrones, M. Doping two-dimensional materials: Ultra-sensitive sensors, band gap tuning and ferromagnetic monolayers. *Nanoscale Horiz.* **2017**, *2*, 72–80. [CrossRef] [PubMed]

14. Qin, X.; Liu, X.; Huang, W.; Bettinelli, M.; Liu, X. Lanthanide-Activated Phosphors Based on 4f-5d Optical Transitions: Theoretical and Experimental Aspects. *Chem. Rev.* **2017**, *117*, 4488–4527. [CrossRef]

15. Gai, S.; Li, C.; Yang, P.; Lin, J. Recent progress in rare earth micro/nanocrystals: Soft chemical synthesis, luminescent properties, and biomedical applications. *Chem. Rev.* **2014**, *114*, 2343–2389. [CrossRef] [PubMed]

16. Bai, G.; Yuan, S.; Zhao, Y.; Yang, Z.; Choi, S.Y.; Chai, Y.; Yu, S.F.; Lau, S.P.; Hao, J. 2D Layered Materials of Rare-Earth Er-Doped MoS2 with NIR-to-NIR Down- and Up-Conversion Photoluminescence. *Adv. Mater.* **2016**, *28*, 7472–7477. [CrossRef] [PubMed]

17. Zhao, Q.; Lu, Q.; Liu, Y.; Zhang, M. Two-dimensional Dy doped MoS2 ferromagnetic sheets. *Appl. Surf. Sci.* **2019**, *471*, 118–123. [CrossRef]

18. Ouma, C.N.M.; Singh, S.; Obodo, K.O.; Amolo, G.O.; Romero, A.H. Controlling the magnetic and optical responses of a MoS2 monolayer by lanthanide substitutional doping: A first-principles study. *Phys. Chem. Chem. Phys.* **2017**, *19*, 25555–25563. [CrossRef]

19. Majid, A.; Imtiaz, A.; Yoshiya, M. A density functional theory study of electronic and magnetic properties of rare earth doped monolayered molybdenum disulphide. *J. Appl. Phys.* **2016**, *120*, 142124. [CrossRef]

20. Zhang, Z.; Zhao, H.; Zhang, C.; Luo, F.; Du, Y. Rare-earth-incorporated low-dimensional chalcogenides: Dry-method syntheses and applications. *InfoMat* **2020**, *2*, 466–482. [CrossRef]

21. Lyu, Y.; Wu, Z.; Io, W.F.; Hao, J. Observation and theoretical analysis of near-infrared luminescence from CVD grown lanthanide Er doped monolayer MoS2 triangles. *Appl. Phys. Lett.* **2019**, *115*, 153105. [CrossRef]

22. Xu, D.; Chen, W.; Zeng, M.; Xue, H.; Chen, Y.; Sang, X.; Xiao, Y.; Zhang, T.; Unocic, R.R.; Xiao, K.; et al. Crystal-Field Tuning of Photoluminescence in Two-Dimensional Materials with Embedded Lanthanide Ions. *Angew. Chem. Int. Ed. Engl.* **2018**, *57*, 755–759. [CrossRef] [PubMed]

23. Radisavljevic, B.; Radenovic, A.; Brivio, J.; Giacometti, V.; Kis, A. Single-layer MoS2 transistors. *Nat. Nanotechnol.* **2011**, *6*, 147–150. [CrossRef]

24. Yang, Y.; Pu, H.; Di, J.; Zang, Y.; Zhang, S.; Chen, C. Synthesis and characterization of monolayer Er-doped MoS2 films by chemical vapor deposition. *Scr. Mater.* **2018**, *152*, 64–68. [CrossRef]

25. Chae, W.H.; Cain, J.D.; Hanson, E.D.; Murthy, A.A.; Dravid, V.P. Substrate-induced strain and charge doping in CVD-grown monolayer MoS2. *Appl. Phys. Lett.* **2017**, *111*, 143106. [CrossRef]

26. Jeon, J.; Jang, S.K.; Jeon, S.M.; Yoo, G.; Jang, Y.H.; Park, J.H.; Lee, S. Layer-controlled CVD growth of large-area two-dimensional MoS2 films. *Nanoscale* **2015**, *7*, 1688–1695. [CrossRef]

27. Zhang, K.; Peng, M.; Wu, W.; Guo, J.; Gao, G.; Liu, Y.; Kou, J.; Wen, R.; Lei, Y.; Yu, A.; et al. A flexible p-CuO/n-MoS2 heterojunction photodetector with enhanced photoresponse by the piezo-phototronic effect. *Mater. Horiz.* **2017**, *4*, 274–280. [CrossRef]

28. Zhang, K.; Peng, M.; Yu, A.; Fan, Y.; Zhai, J.; Wang, Z.L. A substrate-enhanced MoS2 photodetector through a dual-photogating effect. *Mater. Horiz.* **2019**, *6*, 826–833. [CrossRef]

29. Şar, H.; Özden, A.; Demiroğlu, İ.; Sevik, C.; Perkgoz, N.K.; Ay, F. Long-Term Stability Control of CVD-Grown Monolayer MoS2. *Phys. Status Solidi. RRL* **2019**, *13*, 1800687. [CrossRef]

30. Lee, C.; Yan, H.; Brus, L.; Heinz, T.; Hone, J.; Ryu, S. Anomalous Lattice Vibrations of Single-and Few-Layer MoS2. *ACS Nano* **2010**, *4*, 2695–2700. [CrossRef] [PubMed]

31. Paul, K.K.; Mawlong, L.P.L.; Giri, P.K. Trion-Inhibited Strong Excitonic Emission and Broadband Giant Photoresponsivity from Chemical Vapor-Deposited Monolayer MoS2 Grown in Situ on TiO2 Nanostructure. *ACS Appl. Mater. Interfaces* **2018**, *10*, 42812–42825. [CrossRef]

32. Michail, A.; Delikoukos, N.; Parthenios, J.; Galiotis, C.; Papagelis, K. Optical detection of strain and doping inhomogeneities in single layer MoS$_2$. *Appl. Phys. Lett.* **2016**, *108*, 173102. [CrossRef]
33. Zhang, S.; Hill, H.M.; Moudgil, K.; Richter, C.A.; Hight Walker, A.R.; Barlow, S.; Marder, S.R.; Hacker, C.A.; Pookpanratana, S.J. Controllable, Wide-Ranging n-Doping and p-Doping of Monolayer Group 6 Transition-Metal Disulfides and Diselenides. *Adv. Mater.* **2018**, *30*, 1802991. [CrossRef]
34. Ganta, D.; Sinha, S.; Haasch, R.T. 2D Material Molybdenum Disulfide Analyzed by XPS. *Surf. Sci. Spectra* **2014**, *21*, 19–27. [CrossRef]
35. Peterson, P.F.; Olds, D.; Savici, A.T.; Zhou, W. Advances in utilizing eVent based data structures for neutron scattering experiments. *Rev. Sci. Instrum.* **2018**, *89*, 093001. [CrossRef]
36. Han, W.; Li, Z.; Li, M.; Li, W.; Zhang, M.; Yang, X.; Sun, Y. Reductive extraction of lanthanides (Ce,Sm) and its monitoring in LiCl KCl/Bi Li system. *J. Nucl. Mater.* **2019**, *514*, 311–320. [CrossRef]
37. Lopez-Sanchez, O.; Lembke, D.; Kayci, M.; Radenovic, A.; Kis, A. Ultrasensitive photodetectors based on monolayer MoS$_2$. *Nat. Nanotechnol.* **2013**, *8*, 497–501. [CrossRef]
38. Liu, B.; Chen, L.; Liu, G.; Abbas, A.N. High-performance chemical sensing using Schottky-contacted chemical vapor deposition grown monolayer MoS$_2$ transistors. *ACS Nano* **2014**, *8*, 5304–5314. [CrossRef] [PubMed]
39. Jariwala, D.; Sangwan, V.K.; Late, D.J.; Johns, J.E.; Dravid, V.P.; Marks, T.J.; Lauhon, L.J.; Hersam, M.C. Band-like transport in high mobility unencapsulated single-layer MoS$_2$ transistors. *Appl. Phys. Lett.* **2013**, *102*, 173107. [CrossRef]
40. Zhang, F.; Appenzeller, J. Tunability of short-channel effects in MoS$_2$ field-effect devices. *Nano Lett.* **2015**, *15*, 301–306. [CrossRef]
41. Kim, C.; Moon, I.; Lee, D.; Choi, M.S.; Ahmed, F.; Nam, S.; Cho, Y.; Shin, H.J.; Park, S.; Yoo, W.J. Fermi Level Pinning at Electrical Metal Contacts of Monolayer Molybdenum Dichalcogenides. *ACS Nano* **2017**, *11*, 1588–1596. [CrossRef] [PubMed]
42. Kalanyan, B.; Kimes, W.A.; Beams, R.; Stranick, S.J.; Garratt, E.; Kalish, I.; Davydov, A.V.; Kanjolia, R.K.; Maslar, J.E. Rapid Wafer-Scale Growth of Polycrystalline 2H-MoS$_2$ by Pulsed Metalorganic Chemical Vapor Deposition. *Chem. Mater.* **2017**, *29*, 6279–6288. [CrossRef] [PubMed]